

Megapixel time-gated SPAD image sensor for 2D and 3D imaging applications

KAZUHIRO MORIMOTO,^{1,2,*} ANDREI ARDELEAN,¹ MING-LO WU,¹ ARIN CAN ULKU,¹ IVAN MICHEL ANTOLOVIC,¹ CLAUDIO BRUSCHINI,¹ AND EDOARDO CHARBON¹

¹Advanced Quantum Architecture Laboratory (AQUA), Ecole polytechnique fédérale de Lausanne (EPFL), 2002 Neuchâtel, Switzerland

²Device Research & Design Department, Canon Inc., 212-8602 Kanagawa, Japan

*Corresponding author: morimoto.kazuhiro@mail.canon

Received 3 January 2020; revised 10 March 2020; accepted 16 March 2020 (Doc. ID 386574); published 16 April 2020

We present a 1 Mpixel single-photon avalanche diode camera featuring 3.8 ns time gating and 24 kfps frame rate, fabricated in 180 nm CMOS image sensor technology. We designed two pixels with a pitch of 9.4 μm in 7 T and 5.75 T configurations respectively, achieving a maximum fill factor of 13.4%. The maximum photon detection probability is 27%, median dark count rate is 2.0 cps, variation in gating length is 120 ps, position skew is 410 ps, and rise/fall time is <550 ps, all FWHM at 3.3 V excess bias. The sensor was used to capture 2D/3D scenes over 2 m with resolution (least significant bit) of 5.4 mm and precision better than 7.8 mm (rms). We demonstrate extended dynamic range in dual exposure operation mode and show spatially overlapped multi-object detection in single-photon time-gated time-of-flight experiments. © 2020 Optical Society of America under the terms of the [OSA Open Access Publishing Agreement](#)

<https://doi.org/10.1364/OPTICA.386574>

1. INTRODUCTION

Time-resolved imaging sensors enable a number of vision techniques, such as time-of-flight (ToF) imaging, time-resolved Raman spectroscopy, fluorescence lifetime imaging microscopy, super-resolution microscopy, etc. [1–3]. Time-resolved single-photon imaging sensors enable, in addition, quantum vision techniques, such as ghost imaging, sub-shot-noise imaging, quantum LiDAR, quantum distillation, etc. [2,4,5]. Common to these applications is the need for single-photon detection and high timing resolution with low noise and high sensitivity. An important limitation in the majority of the implementations has been the image sensor, usually made of a single pixel or at most a 1 kpixel array. Thus, a larger format picture requires 1D or 2D scanning, thereby curtailing the frame rate, which is limited by the speed of the scanner. In addition, scanners may be bulky and add another level of complexity to the imaging system. To address these issues, researchers have recently created large-format cameras with a single-photon avalanche diode (SPAD) in each pixel and time-gating or time-to-digital converters (TDCs) on chip [6–10]. Though, the crux of a large-format camera remains the pixel pitch and the amount of functionality per pixel. Researchers have thus resorted to 3D integration using backside-illuminated SPADs on the top tier and control/processing/readout electronics on the bottom tier [11–14].

Recently, a novel photon-counting image sensor called the quanta image sensor (QIS) has been demonstrated [15–17]. Single-photon sensitivity without avalanche gain is achieved in the QIS with pixels having sub-0.5e⁻ rms read noise as a result of a high conversion gain. QISs inherit several advantages of CMOS

image sensors, such as a potentially small pixel size, high spatial resolution, low dark current, high quantum efficiency, and low power consumption. A spatial resolution of up to 1 megapixel with 1.1 μm pixels has been reported in a QIS [18,19], enabling low noise and high dynamic range imaging for scientific, space, and security applications. A limitation of the QIS technology, though, is timing resolution. The finite time required for charge transfer in the pixels and sequential scanning readout prevent QISs from detecting timing information below 1 μs . SPADs, in contrast, enable single-photon detection with a timing resolution of up to few tens of picoseconds owing to the fast avalanche multiplication process. While a TDC-based approach enables precise time stamping of the detected photons in a SPAD array, it is not suited for scaling due to large circuit area and high power dissipation [20–24]. Our time-gating approach, in contrast to [6–9], entails less than eight transistors, and is promising for scalable photon counting image sensors toward sub-100-ps timing resolution and megapixel sensor resolution. In this paper, we advocate the use of this approach to achieve large-format time-gated SPAD sensors capable of high timing resolution and small pixel pitch.

2. IN-PIXEL TIME GATING

In-pixel time-gating approaches involve compact pixel circuits. They are therefore well-suited for the implementation of large-scale time-resolved SPAD sensors with low power dissipation. Figure 1(a) illustrates the operation principle of time-gated ToF ranging. Laser pulses are repeatedly sent toward the target; the reflected photons are detected at the sensor with a delay of Δt .

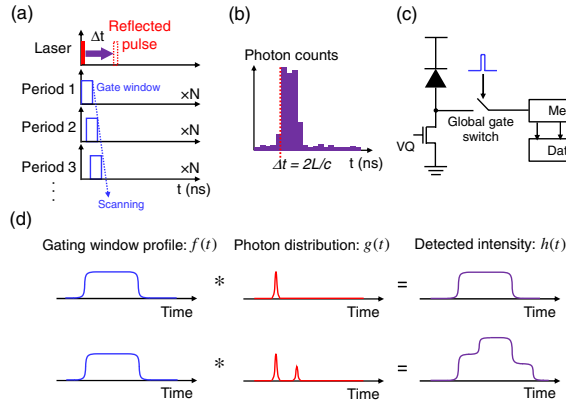


Fig. 1. Conceptual views of time-gated ToF ranging. (a) Pixel circuit architecture of time-gated SPAD sensor. (b) Timing diagram of ToF ranging based on time gate scanning, where N is the number of repeated measurements in a single period. (c) Expected photon count distribution as a function of gate position. (d) Schematic views of the gating window profile, photon distribution, and measured intensity over time with single reflective object (top) and double reflective objects (bottom).

Typical time-gating measurements involve consecutive frames with a finely shifted gate window, each of which performs photon counting integrated over N sub-frames. Finer gate scanning improves timing resolution, while sacrificing depth measurement rate or range. From these measurements, a histogram may be derived, as shown in Fig. 1(b). Photon counts in a histogram bin include background photon counts and dark counts when the reflected laser pulse is outside of the gate window, whereas the photon counts are offset by the reflected laser signal captured within the gate window. When the peak intensity of the reflected signal is higher than the background photon counts, the resulting photon count profile for each pixel forms a rectangular distribution with its width corresponding to the gate window length. The delay time Δt can be extracted from either the rising or falling edge of this profile, while distance L from the detector to the target is estimated by

$$L = \frac{c\Delta t}{2}, \quad (1)$$

where c is the speed of light. Figure 1(c) shows a simplified schematic of a time-gated SPAD pixel. The SPAD is connected to a quenching transistor to limit self-sustained avalanche breakdown, and its output signal is selectively fed to an in-pixel memory when a global gate switch is activated. The gate control pulse can be as short as a few nanoseconds and is synchronized with repetitive laser pulse emissions toward target objects. The stored signal is read out through a fast data I/O circuit.

More generally, the detected intensity profile $h(t)$ in a given measurement time frame is formulated by the convolution of two functions:

$$h(t) = f(t) * g(t), \quad (2)$$

where $f(t)$ is the gating window profile and $g(t)$ is the photon probability density function. Note that $h(t)$ yields a , when integrated from $-\infty$ to $+\infty$, where a is the total detected photon count in the measurement time frame. Figure 1(d) shows the detected intensity profile of photons captured by the detector characterized by $f(t)$. When the photon probability density function

can be approximated by a single Gaussian distribution with a sufficiently small standard deviation, if compared to the gate length, the intensity profile can be expressed as

$$h(t) \approx f(t) * a \delta(t - \Delta t) = a f(t - \Delta t), \quad (3)$$

where a and Δt are the photon count and delay time of the Gaussian peak, respectively, and δ is the Dirac delta function as an approximated form of a narrow Gaussian distribution. In practice, the detected intensity profile can take more complicated forms. For instance, when the target object is imaged through semi-transparent (semi-reflective) materials such as glass, plastics, or liquids, the photon distribution can be expressed as a superposition of multiple Gaussian functions with different peak heights and positions. Assuming again negligible standard deviation, the detected intensity profile is

$$h(t) \approx f(t) * \left[\sum_i a_i \delta(t - \Delta t_i) \right] = \sum_i a_i f(t - \Delta t_i), \quad (4)$$

where a_i and Δt_i are the photon count and delay time of the i th Gaussian peak, respectively. Equation (4) suggests that the multiple reflection results in a superposition of multiple gating window functions, each having different height and delay. An example with two reflective peaks in the photon distribution is shown in the bottom of Fig. 1(d).

Note that when $h(t)$ is measured and $f(t)$ is known, a full profile of $g(t)$ can thus be obtained by deconvolution. In a real situation, $h(t)$ can be distorted by non-ideal effects, such as photon-shot noise, ambient light, dark counts, afterpulsing, cross talk, timing jitter, etc. Those effects can introduce noise in the deconvolution. In ToF ranging, however, the assumption for reflected laser pulses to have negligibly narrow widths is valid in most cases. This assumption simplifies the process of distance calculation, where the time-of-arrival information can be readily extracted by finding the rising or falling edges in the measured intensity profile.

3. SENSOR ARCHITECTURE

In this paper, we present the first 1 Mpixel camera based on the SPAD pixel described above, with a pitch of 9.4 μm . We propose two architectures for the pixel: 7 T (7 transistors per pixel) for pixel A and 5.75 T (5.75 transistors per pixel on average) for pixel B without and with readout transistor sharing, respectively. The pixels achieve fill factors of 7.0% and 13.4%, respectively; both pixels use a dynamic memory to store single-photon events generated by the SPAD. Binary photon counting images are captured and streamed out at 24,000 fps (maximum), corresponding to a total data rate of 25 Gbps.

Figures 2(a) and 2(b) show the schematics and timing diagrams of both pixels (see Supplementary Notes S1 and S2 of [Supplement 1](#) for more information). The feedback loop in pixel B prevents any subsequent avalanches within a frame; this is advantageous in very large arrays, since it reduces the current drawn from the cathode voltage node V_{OP} and thus the power dissipation from that node, which, given the high voltages used, can be significant for pixel counts above 100,000. In our chip, under strong illumination, the current drawn from V_{OP} by pixel A is over 400 \times that drawn from pixel B (see Supplementary Note S3 of [Supplement 1](#)).

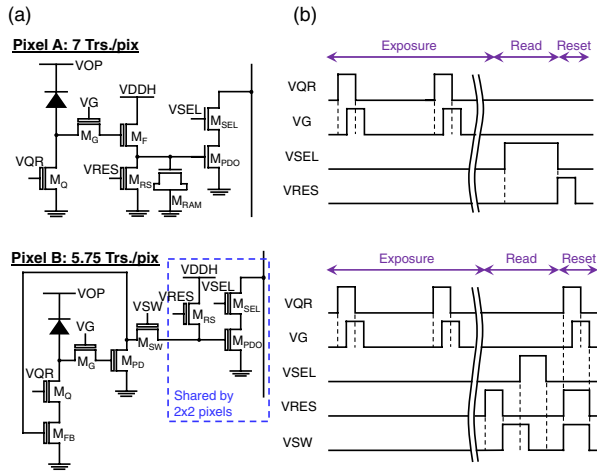


Fig. 2. Schematic views of designed SPAD pixels. (a) Pixel circuit schematics for pixel A and pixel B. Pixel A consists of thick- and thin-oxide transistors, whereas pixel B consists only of thick-oxide transistors. (b) Timing charts for pixel circuit operation.

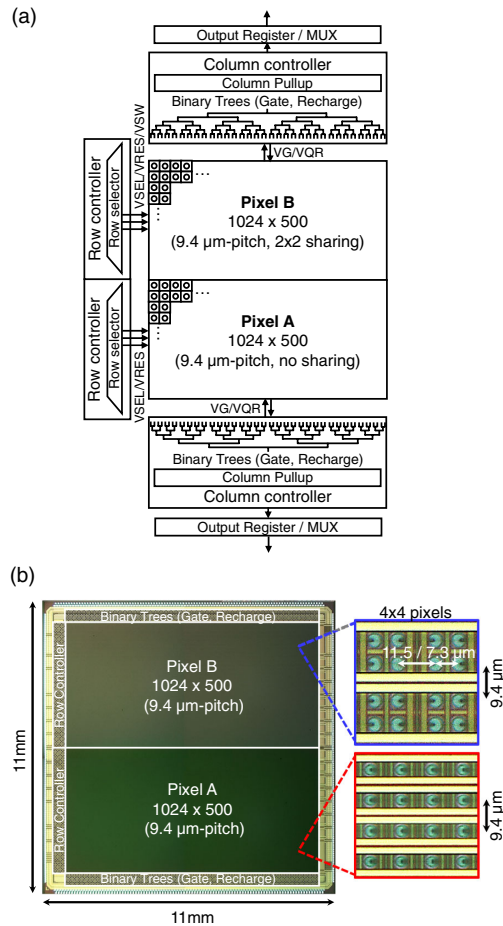


Fig. 3. 1 Mpixel time-gated SPAD image sensor architecture. (a) Sensor block diagram. (b) Chip micrograph and magnified views of pixel arrays.

The camera block diagram is shown in Fig. 3(a); it comprises two independent sections of 1024 × 500 pixels, where the bottom half array is based on pixel A and the top half on pixel B. A dual

binary tree controls the time gate, which reaches a minimum length of 3.8 ns (tunable up to 9.6 ns), and its variation of 120 ps (FWHM). Each row is read out in 83 ns and stored in a 1024-bit and a 512-bit output register for pixel A and pixel B, respectively, at the chip bottom and top. A multiplexer scans it in 128-bit words, which are then transferred off-chip via 128 I/O pins (each half) by way of a dual parallel bus, thus achieving a frame rate of 24 kfps. The micrograph of the image sensor is shown in Fig. 3(b). The active area is drawn circular, and the drawn active diameters for pixels A and B are 2.8 μm and 3.88 μm, respectively.

Unless otherwise noted, all of the following experiments are performed in global shutter mode with 42 μs readout per binary frame.

4. EXPERIMENTAL RESULTS

A. DCR and PDP

Figure 4(a) shows the room temperature (RT) cumulative dark count rate (DCR) probability distribution of the SPADs throughout the chip, with a median of 0.4 cps (pixel A) and 2.0 cps (pixel B) at an excess bias of 3.3 V. The corresponding DCR per unit drawn active area is 0.065 cps/μm² for pixel A and 0.17 cps/μm² for pixel B. These DCR density metrics are equal to or better than state-of-the-art SPAD devices [25,26]. Figure 4(b) shows the measured median DCR as a function of excess bias at room temperature. Figure 4(c) shows the measured photon detection probability (PDP) as a function of wavelength. A maximum PDP of 10.5% (pixel A) and 26.7% (pixel B) is reached at 520 nm at the same excess bias of 3.3 V, while the PDP non-uniformity is better than 1.4% (pixel A) and 3.2% (pixel B) at RT. Lower PDP compared to the previous work based on p-i-n SPAD [25] is caused by typical border effects [27]. The border effects are more significant when the active diameter is smaller than 5 μm. Figure 4(d) shows the maximum PDP as a function of the excess bias, whereas the dotted lines are guides for the eye. (see Supplementary Note S4 of [Supplement 1](#) for more detailed analysis).

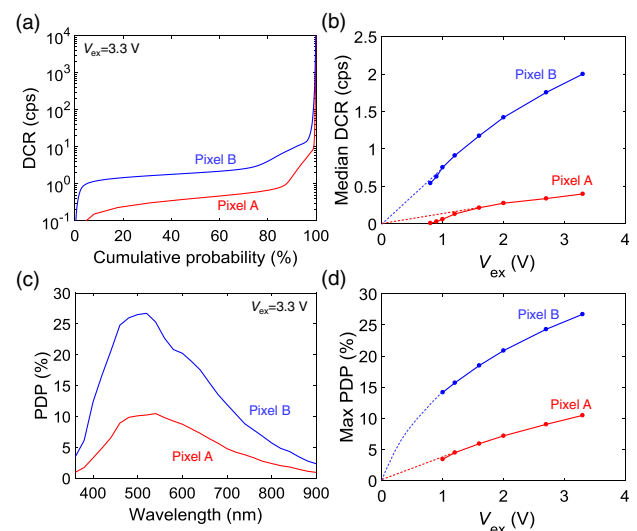


Fig. 4. Measured DCR and PDP for pixels A and B. (a) Room temperature cumulative histogram of DCR at excess bias of 3.3 V. (b) Excess bias dependence of median DCR at room temperature. (c) Wavelength dependence of PDP at an excess bias of 3.3 V. (d) Excess bias dependence of maximum PDP at room temperature.

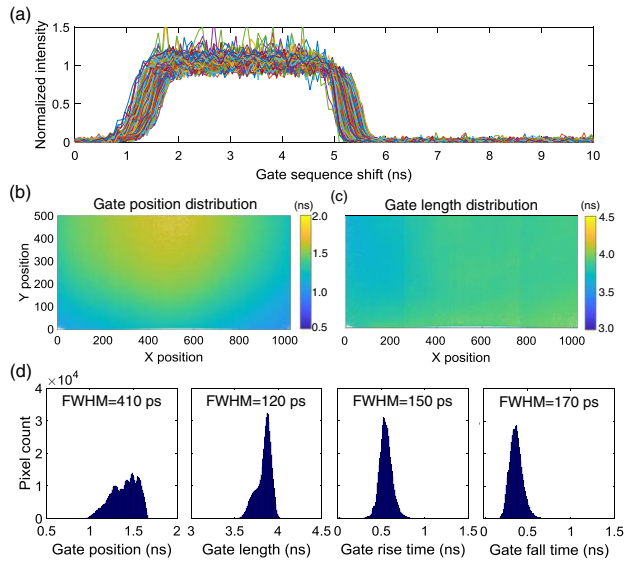


Fig. 5. Measured time-gating performance for pixel A. (a) Gate window profiles for uniformly sampled 160 pixels. (b) Color plot of gate position distribution over 1024×500 pixels. (c) Color plot of gate length distribution over 1024×500 pixels. (d) Histograms for gate position, gate length, rise time, and fall time.

B. Time-Gating Performance

The timing performance of pixel A was characterized in Fig. 5. A 785 nm laser pulsed at 25 MHz (average power: 5 mW, optical pulse width: 80 ps FWHM, ALS GmbH, Berlin, Germany) illuminates the whole array, while the time gate window is continuously shifted with respect to the laser trigger by steps of 36 ps over a range of 10 ns. For each gate position, 255 binary frames are acquired and summed in a Kintex 7 FPGA (Xilinx Inc., San Jose, California, USA) to generate an 8-bit image. Figure 5(a) shows the gate window profiles for 160 pixels uniformly sampled from the bottom-left to the top-right of the pixel array. Broadening of rising and falling edges indicates the non-uniformity of gate signal propagation over the pixel array. Figures 5(b) and 5(c) demonstrate the spatial uniformity of gate position and gate length. The gate and recharge signals injected from the bottom side of the array require more time to propagate and activate the gate of the pixels in the top of the array. Horizontal skew of the gate position in the top side of the array stems from the asymmetry of power routing where the power and ground are supplied from the left, right, and bottom sides, but not from the top side of the array. The gate length distribution shows better uniformity than the gate position distribution. Note that white pixels in the color plots indicate that the measured timing is out of range with respect to the color bar. Figure 5(d) shows the histograms of gate position, gate length, rise time, and fall time. The gate position skews and variation in gate length were measured as 410 ps and 120 ps (FWHM), respectively, while an average gate length of 3.8 ns was achieved. These values include the laser pulse width of 80 ps FWHM.

C. 2D Imaging

The chip was tested as an intensity image sensor with a standard chart. Figure 6(a) shows a schematic view of the experimental setup. Figure 6(b) shows a 1 Mpixel monochrome image obtained at 24 kfps with a uniform illumination of 50 lx (indoors). For each

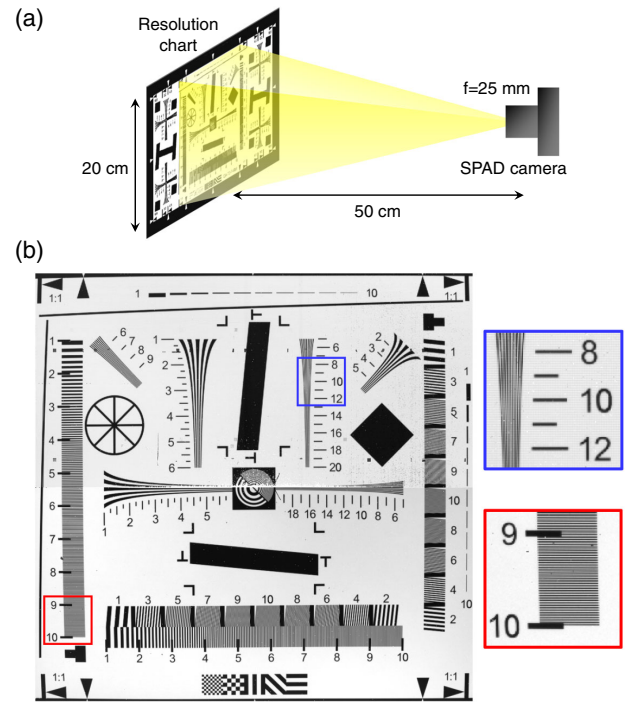


Fig. 6. 2D intensity imaging of a standard test chart with 1 Mpixel resolution. (a) Experimental setup. (b) A 14-bit image obtained by summing 16,320 binary images. Magnified views of two small areas, indicated by blue and red squares, are shown on the right.

half, 16,320 binary images are taken in rolling shutter mode and are summed to acquire a 14-bit intensity image. Exposure time is set at 2 s to compensate the smaller aperture size for wide depth of field. The image contrast for the top and bottom half is tuned independently to compensate the difference in the photon detection efficiency (PDE). On the right side of Fig. 6(b), the magnified images show that the line patterns are well-resolved, up to number 10 in the chart, indicating the spatial resolution of 1000 dots within the horizontal and vertical fields of view.

The dynamic range of a 2D image sensor is critical for a wide range of applications. Recently, a method to extend the dynamic range by mixing multiple different exposure times in a single frame has been reported for SPAD-based binary image sensors [28]. Compared to the case with fixed single exposure time for all the binary frames, mixing multiple exposure times results in slower saturation of the output counts when increasing the incident photon flux, giving richer tones for high illumination conditions. Yet, dynamic range extension based on interleaved multiple exposures in a SPAD sensor is reported only for a limited sensor resolution of 96×40 pixels. In addition, incident photon count dependencies of output signal, noise, and SNR have not yet been systematically compared between single and multiple exposure modes under equalized total exposure conditions.

Figure 7(a) shows the timing sequences of single and dual exposure modes in a time-gated SPAD sensor. The sensor is operated in global shutter mode; each shaded region in the figure represents a global exposure, followed by sequential readout of a full-resolution binary frame. A set of streamed binary frames is integrated in the FPGA to construct one N -bit image. In single exposure mode, the global exposure time is fixed over one N -bit frame. In dual exposure mode, short and long global exposures are staggered to form

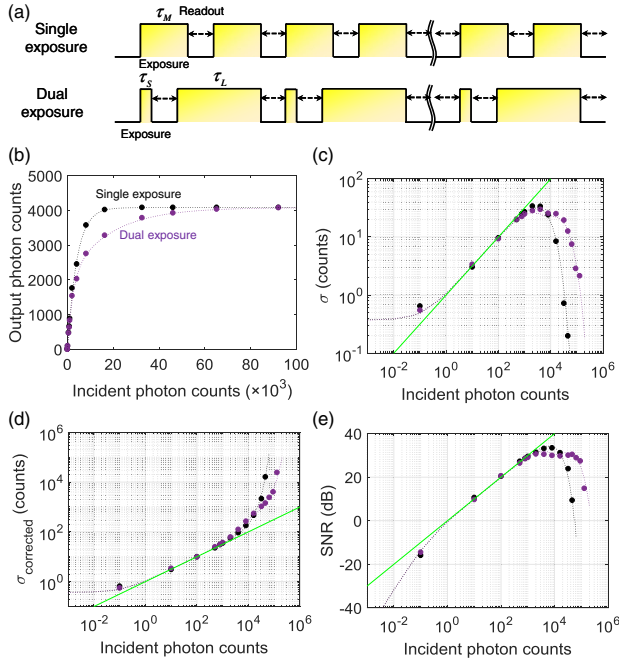


Fig. 7. Conceptual view and measured or simulated results for the dynamic range extension technique. (a) Timing diagrams of single and dual exposure modes. (b) Measured (markers) and fitted (dotted lines) output photon counts as a function of incident photon counts for pixel A. (c) Measured (markers) and Monte Carlo-simulated (dotted lines) standard deviation. (d) Measured and simulated standard deviation after linearity correction. (e) Measured and simulated SNR. Green lines indicate the photon-shot noise limit.

one N -bit image. In this experiment, the ratio between short exposure time τ_S and long exposure time τ_L for dual exposure mode is set at 1 to 8, whereas the exposure time τ_M for single exposure mode is set at $4.5\tau_S$. For systematic comparison of the two operation modes, maximum photon counts and total exposure time in a single N -bit frame are set equal for the two modes: $2\tau_M = \tau_S + \tau_L$.

Figure 7(b) shows the measured output photon counts as a function of incident photon counts for single and dual exposure modes. 4080 binary frames are summed to form a 12-bit image. τ_S is set to 121 μ s, whereas the readout of a binary frame takes 42 μ s. The total exposure time is 2.2 s for both single and dual exposure modes. Dotted lines are the fitted curves for each mode based on the following equations:

$$N_{out}^S = N_{sat} \times \left(1 - e^{-\frac{N_{in}}{N_{sat}}}\right), \quad (5)$$

$$N_{out}^D = \frac{N_{sat}}{2} \times \left[\left(1 - e^{-\frac{2\tau_L}{(\tau_L + \tau_S)} \cdot \frac{N_{in}}{N_{sat}}}\right) + \left(1 - e^{-\frac{2\tau_S}{(\tau_L + \tau_S)} \cdot \frac{N_{in}}{N_{sat}}}\right) \right], \quad (6)$$

where N_{out}^S and N_{out}^D are the output counts in the single and dual exposure modes, respectively, N_{sat} is 4080, and N_{in} is the incident photon count per one N -bit frame. The fitted curves are in good agreement with the trends of measured output counts. The output counts of the dual exposure mode saturate later than those of the single exposure mode, indicating the extended dynamic range.

Figure 7(c) shows the standard deviation of measured outputs as a function of incident photon counts. Raw output counts of

100 pixels in the center of the array are used to calculate the standard deviation, whereas the photon-shot noise limit is also shown. In the lower incident photon counts, the measured standard deviation is higher than the shot noise limit due to the contribution from DCR non-uniformity. Under intermediate photon counts, the measured standard deviation follows the shot noise limit. For higher incident photon counts, the measured standard deviation is lower than the shot noise limit due to the compression of the output signal when a saturation of 4080 counts is reached [29]. To reproduce the output characteristics, a Monte Carlo simulation was performed based on Poissonian statistics of the incident photons and dark counts for each binary frame. The simulation results for two modes are shown as dotted curves, which are highly consistent with the measured trends.

In real situations, non-linear output characteristics in Fig. 7(b) have to be corrected to ensure the natural contrast for human eyes. Figure 7(d) shows the measured standard deviation based on corrected output counts. Similar to the trends in Fig. 7(c), the deviation from photon-shot noise limit is observed in the lower incident photons due to the DCR non-uniformity, and the deviation is suppressed for intermediate photon counts. For the higher incident photons, the measured trends go above the shot noise limit. The difference with respect to the uncorrected curves of Fig. 7(c) arises from the amplification of photon-shot noise in the linearity correction process. Again, Monte Carlo simulations (dotted lines) precisely reproduce the measured results for both operation modes. The noise increase in the dual exposure mode is observed later than that of the single exposure mode, which is a direct consequence of dynamic range extension.

Figure 7(e) shows the measured SNR plots for the two exposure modes. The dynamic range, defined as a ratio of input-referred photon counts for 99% of saturation counts to dark counts, was measured at 96.3 dB for single exposure and 108.1 dB for dual exposure. A 11.8 dB improvement is demonstrated with equal maximum counts and total exposure time. The highest SNR for single and dual exposure is 33.3 dB and 30.5 dB, respectively.

In Fig. 8, the effect of the dynamic range extension is investigated in a real-life scene. In the single exposure mode, the background scene is overexposed [Fig. 8(a)], while the gray-scale tone of the scene is clearly visible in the dual exposure mode

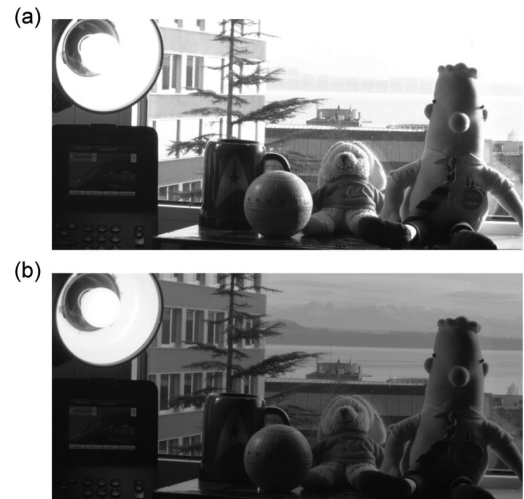


Fig. 8. 2D images of a real-life scene captured with pixel A: (a) 18-bit image taken in single exposure mode; (b) 18-bit image taken in dual exposure mode.

[Fig. 8(b)]. The difference in the maximum SNR is too small to be recognized.

D. 3D Imaging

Figures 9(a) and 9(b) show a 2D and a color-coded 3D picture obtained by illuminating a scene with a 637-nm laser pulsed at 40 MHz (average power: 2 mW, optical pulse width: 80 ps FWHM, ALS GmbH, Berlin, Germany) and captured on the half-resolution image sensor (pixel A). The gate window with its length of 3.8 ns is shifted from 0.6 ns to 13.2 ns by steps of 36 ps to acquire full photon intensity profiles as a function of the gate position. The distance least significant bit in this measurement corresponds to 5.4 mm. The intensity profile for each pixel is smoothed by taking the moving average over gate positions to suppress the effect of photon-shot noise. The depth information is reconstructed by detecting the rising edge position of the smoothed intensity profile for each pixel, corresponding to the time-of-arrival of the reflected laser pulse. The gate timing skew over the array is compensated by subtracting the background distribution shown in Fig. 5(b) from the measured time-of-arrival distribution. In Fig. 9(b), the red color denotes higher proximity to the SPAD camera, whereas the blue color corresponds to higher distance. The maximum depth range for this measurement was set to 2 m, but it can be extended to tens of meters by lowering the laser repetition frequency and increasing the gate step. Note that some pixels in the scene show “no data” (black) due to laser speckle patterns, leading to locally insufficient photon counts for distance estimation. The fine gate scanning pitch and long exposure are used to achieve high depth precision, and the resulting data acquisition time for this measurement was few tens of seconds. This is considerably longer than that of other ranging methods, such as indirect ToF, but it can be readily reduced by increasing the gate scanning pitch, reducing

the scanning range, and increasing the laser power to reduce the exposure time. In addition, further improvement is expected by implementing an on-chip microlens to boost the sensitivity.

Figure 9(c) shows the measured distance as a function of the actual object distance. In Figs. 9(c)–9(e), a flat object covered with white paper (reflectance around 60%) is used to evaluate the measured distance, accuracy, and precision. In Fig. 9(c), the measured distance is extracted by taking the average of the single pixel distance over 20×20 pixels at the center of the array. A very good agreement with the actual distance is observed within the measured range from 0.2 to 1.6 m. In Fig. 9(d), the distance accuracy is calculated as the averaged measured distance subtracted by the actual distance. For the measured distance range, the accuracy is always better than 1 cm. In Fig. 9(e), distance precision is exploited as a standard deviation of the single pixel distance over 20×20 pixels in the center of the array. The precision is better than 7.8 mm (rms) for all the measured points up to 1.6 m.

E. Multi-Object 3D Imaging

Compared to indirect ToF [30–32], direct ToF has the advantage that spatially overlapped multiple reflective objects can be imaged individually and accurately. Multi-object detection has been experimentally demonstrated in SPAD-based direct ToF sensors [33,34], where power- and area-consuming TDC circuits and large computational cost for histogramming severely limited the size of the detector. Multi-object detection has also been demonstrated by either coding temporal illumination or exposure patterns [35,36], which involves a large computational cost to recover 3D images.

A time-gated ToF sensor provides an alternative, scalable solution by means of compact pixel circuitry and less complicated computation. A CMOS-based time-gating scheme has been adopted for multi-object detection in a 160×120 -pixel array [37], where, however, the readout noise limits the lower bound of detectable signal level for each pixel. The readout noise represents

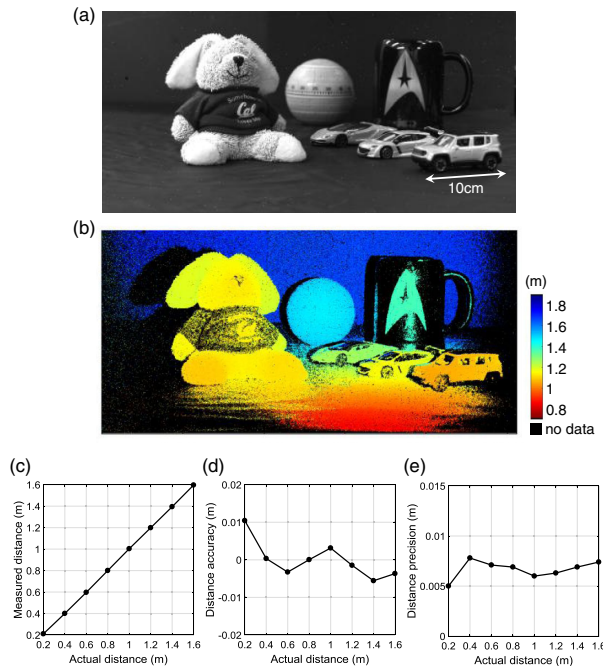


Fig. 9. Measured results for time-gated ToF ranging: (a) real-life 2D intensity image; (b) color-coded 3D image of the same scene obtained with time-gated ToF; (c) measured distance versus actual distance; (d) measured distance accuracy versus actual distance; (e) measured distance precision versus actual distance.

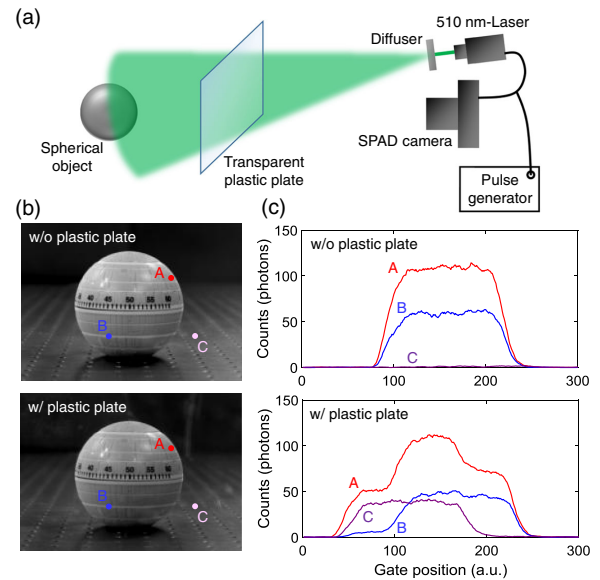


Fig. 10. Experimental setup and measured results for time-gated ToF under multiple reflections. (a) Experimental setup to perform the multi-object detection. (b) Captured 2D images with and without the plastic plate. (c) Measured photon count profiles for three different pixels, with and without the plastic plate.

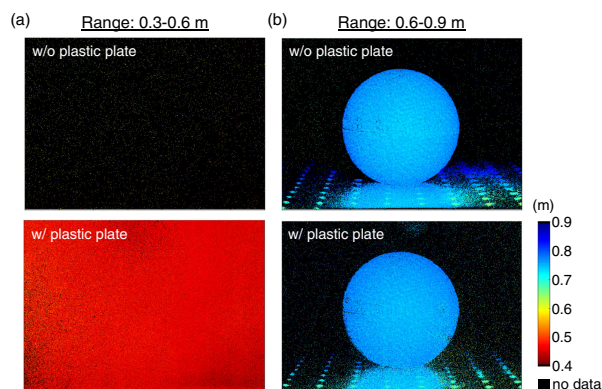


Fig. 11. Reconstructed 3D images in the multi-object detection experiment. (a) 3D images reconstructed based on the distance range of 0.3–0.6 m (central 700×500 pixels cropped). Black color indicates that no laser reflection is detected in the measured range. (b) 3D images reconstructed based on the distance range of 0.6–0.9 m.

a critical issue for scaling the array size because smaller pixel size and larger pixel array size result in the reduced number of reflected photons per pixel, severely limiting SNR. Our gated SPAD pixel enables scalable and readout-noise-free single-photon time gating for multi-object detection.

Figure 10(a) shows the experimental setup: a 510-nm laser beam pulsed at 40 MHz (average power: 2 mW, optical pulse width: 130 ps FWHM, PicoQuant GmbH, Berlin, Germany) is spread by a diffuser and used to illuminate a spherical target. The SPAD camera is synchronized with the laser triggering signal, and a transparent plastic plate is inserted between the camera and the object. The distances from the camera to the plastic plate and the

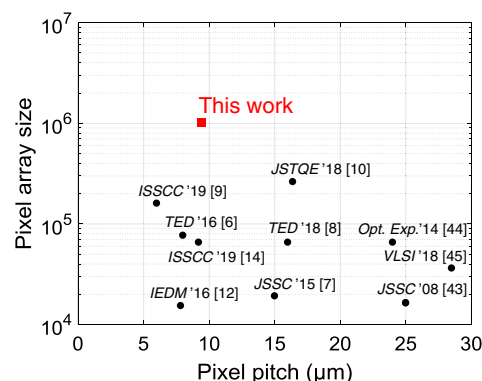


Fig. 12. State-of-the-art comparison of pixel array size and pixel pitch in SPAD sensors [6–10, 12, 13, 43–45], based on published works as of December 2019.

object are 0.45 m and 0.75 m, respectively. Figure 10(b) shows 2D intensity images under indoor lighting with and without the plastic plate inserted. Since the plate is almost transparent, no significant difference is observed in the 2D images for those two cases.

The measured time-gating profiles for three representative points (A, B, and C) are plotted in Fig. 10(c). Without the plate, the time-gating profiles for points A and B show only a single smoothed rectangular function waveform with its rising edge around gate position 100 (one step of the position corresponding to 36 ps). For point C, the photon count stays close to zero over the measured gate position range, indicating no reflective object is detected at this pixel. With the plastic plate, by contrast, the profile at point A shows two-step rising edges around gate positions 40 and 100. Given that the measured profile of photon counts is a

Table 1. State-of-the-Art Comparison of Performance and Specifications in Large-Scale SPAD Arrays, Based on Published Works as of December 2019

	[7]	[6]	[14]	[10]	[9]	This Work (Pixel A/B)
Process technology	350 nm HV CMOS	130 nm CIS	40/90 nm 3D-BSI	180 nm CMOS	65 nm CIS	180 nm CMOS
Chip size (mm ²)	3.42×3.55	3.4×3.1	—	9.5×9.6	—	11×11
Sensor resolution	160×120	320×240	256×256	512×512	400×400	1024×1000
Pixel size (μm)	15	8	9.2	16.38	6	9.4
Fill factor (%)	21	26.8	51	10.5	70	7.0/13.4
Pixel output bit depth	5.4b	1b	14b	1b	1b	1b
No. of pixel transistors	8	9	>600	11	4	7/5.75
Median DCR (cps)	580 ($V_{ex} = 3$ V)	47 ($V_{ex} = 1.5$ V)	20 ($V_{ex} = 1.5$ V)	7.5 ($V_{ex} = 6.5$ V)	100 (—)	0.4/2.0 ($V_{ex} = 3.3$ V)
Max. PDP (%)	—	39.5 ($V_{ex} = 1.5$ V)	23 ($V_{ex} = 3$ V)	50 ($V_{ex} = 6.5$ V)	—	10.5/26.7 ($V_{ex} = 3.3$ V)
Max. PDE (%)	—	10.6 ($V_{ex} = 1.5$ V)	11.7 ($V_{ex} = 3$ V)	5.25 ($V_{ex} = 6.5$ V)	—	0.7/3.6 ($V_{ex} = 3.3$ V)
Cross talk (%)	—	—	—	—	—	0.17/0.39 ($V_{ex} = 3.3$ V)
Min. gate length (ns)	0.75	—	—	5.75	—	3.8
Frame rate (fps)	486 (5.4b)	16,000 (1b)	—	97,700 (1b)	60 (—)	24,000 (1b)
Power dissipation (W)	0.1567	—	0.0776	0.0267	—	0.284/0.535

convolution of a single smoothed rectangular function and the reflected photon intensity distribution, the two-step profile is a convincing evidence of double reflection from the plastic plate and the spherical object. Similar behavior is observed at point B, where the slope of the first rising edge around gate position 40 is milder than that of point A. The profile at point C shows only a single rising edge around gate position 40, corresponding to the reflection from the plastic plate. The variation of the slope for the rising edge around gate position 40 between different points is induced by the non-uniform reflection from the surface of the plastic plate.

Figure 11 shows the reconstructed 3D images based on time-gated ToF. The photon counting profile for each pixel is analyzed to extract the position of rising edges. The rising edge is searched by defining a virtual gate window containing 60 data points of the measured intensity profile. The window is scanned over the whole gate position in a non-overlapping fashion, and the existence or non-existence of a rising edge in the virtual window is determined for each scanning position. Figure 11(a) shows the estimated local distance within the range of 0.3–0.6 m. Black pixels represent no object detected within the range. Without the plastic plate, the vast majority of the pixels show no detection (black), while the majority of the pixels indicate a reflection at 0.45 m (dark red) with the plastic plate, which is consistent with its actual position. Figure 11(b) shows the estimated distance within the range of 0.6–0.9 m. For both cases, the distance map of the spherical target object is reconstructed precisely. The measured target object distance is approximately 0.75 m, which is also consistent with the actual distance.

The results demonstrate the capability of our time-gated SPAD camera to perform spatially overlapped multi-object detection. Note that the proposed scheme can be applied to the detection of more than two reflection peaks. Finer scanning of the virtual gate window in post-processing enables systematic detection of multiple peaks. The minimum resolvable distance between two neighboring reflective materials is fundamentally limited by the finite rising or falling time of the gate window profile, corresponding to 5–10 cm in this SPAD sensor.

5. CONCLUSION

In this paper, a 1 Mpixel time-gated SPAD image sensor is reported for the first time. In SPAD research, achieving a megapixel SPAD sensor has been considered one of the most important milestones for over a decade [38,39]. The sensor is applied to high dynamic range 2D imaging and high spatiotemporal resolution 3D imaging. To the best of our knowledge, the spatially overlapped multi-object detection with the single-photon time-gating scheme has been experimentally demonstrated for the first time. Figure 12 shows a state-of-the-art comparison of SPAD pixel pitch and array size. The array size of our sensor is the largest, almost 4 times higher than that of the state-of-the-art sensor [10], while the pixel pitch is one of the smallest. A more detailed comparison is summarized in Table 1. The median DCR is the lowest among other works thanks to the optimized process and miniaturized active size. The lower fill factor and PDE compared to the prior art and other single-photon detector technologies (Electron-multiplying charge-coupled device, Intensified charge-coupled device, QIS) are due to the front-side illuminated configuration; these figures of merit can be further improved, typically by a factor of 2 to 10, by introducing on-chip microlenses [40–42] (see also Supplementary Note S5 of Supplement 1). Owing to its noise and dynamic range

performance, the proposed sensor will be useful in a wide variety of industrial applications, such as security, automotive, robotic, biomedical, and scientific applications, including quantum imaging and ultra-high-speed imaging.

Funding. Swiss National Science Foundation (166289); Canon Inc.

Acknowledgment. The authors thank the Swiss National Science Foundation for funding, in part, this research.

Disclosures. EC: Fasttree3D SA (I,S) and PI Imaging Technology SA (I,S), CB: PI Imaging Technology SA (I,S), IMA: PI Imaging Technology SA (I,S), and KM: Canon Inc. (F,E). The remaining authors declare no conflicts of interest.

See Supplement 1 for supporting content.

REFERENCES

1. A. Velten, T. Willwacher, O. Gupta, A. Veeraraghavan, M. G. Bawendi, and R. Raskar, "Recovering three-dimensional shape around a corner using ultrafast time-of-flight imaging," *Nat. Commun.* **3**, 745 (2012).
2. M. O'Toole, D. B. Lindell, and G. Wetzstein, "Confocal non-line-of-sight imaging based on light-cone transform," *Nature* **555**, 338–341 (2018).
3. C. Bruschini, H. Homulle, I. M. Antolovic, S. Burri, and E. Charbon, "Single-photon avalanche diode imagers in biophotonics: review and outlook," *Light Sci. Appl.* **8**, 87 (2019).
4. H. Defienne, M. Reichert, J. W. Fleischer, and D. Faccio, "Quantum image distillation," *Sci. Adv.* **5**, eaax0307 (2019).
5. A. Lyons, F. Tonolini, A. Boccini, A. Repetti, R. Henderson, Y. Wiaux, and D. Faccio, "Computational time-of-flight diffuse optical tomography," *Nat. Photonics* **13**, 575–579 (2019).
6. N. A. W. Dutton, I. Gyongy, L. Parmesan, S. Gnechchi, N. Calder, B. R. Rae, S. Pellegrini, L. A. Grant, and R. K. Henderson, "A SPAD-based QVGA image sensor for single-photon counting and quanta imaging," *IEEE Trans. Electron Devices* **63**, 189–196 (2016).
7. M. Perenzoni, N. Massari, D. Perenzoni, L. Gasparini, and D. Stoppa, "A 160×120-pixel analog-counting single-photon imager with time-gating and self-referenced column-parallel A/D conversion for fluorescence lifetime imaging," *IEEE J. Solid-State Circuits* **51**, 155–167 (2016).
8. I. Gyongy, N. Calder, A. Davies, N. A. W. Dutton, R. R. Duncan, C. Rickman, P. Dalgarno, and R. K. Henderson, "A 256×256, 100-kfps, 61% fill-factor SPAD image sensor for time-resolved microscopy applications," *IEEE Trans. Electron Devices* **65**, 547–554 (2018).
9. Y. Hirose, S. Koyama, T. Okino, A. Inoue, S. Saito, Y. Nose, M. Ishii, S. Yamahira, S. Kasuga, M. Mori, T. Kabe, K. Nakanishi, M. Usuda, A. Odagawa, and T. Tanaka, "A 400×400-pixel 6-μm-pitch vertical avalanche photodiodes CMOS image sensor based on 150 ps-fast capacitive relaxation quenching in Geiger mode for synthesis of arbitrary gain images," in *IEEE Int. Solid-State Circuits Conference* (2019).
10. A. C. Ulku, C. Bruschini, I. M. Antolovic, Y. Kuo, R. Ankri, S. Weiss, X. Michalet, and E. Charbon, "A 512×512 SPAD image sensor with integrated gating for widefield FLIM," *IEEE J. Sel. Top. Quantum Electron.* **25**, 1–12 (2019).
11. J. M. Pavia, M. Scandini, S. Lindner, M. Wolf, and E. Charbon, "A 1 × 400 backside-illuminated SPAD sensor with 49.7 ps resolution, 30 pJ/sample TDCs fabricated in 3D CMOS technology for near-infrared optical tomography," *IEEE J. Solid-State Circuits* **50**, 2406–2418 (2015).
12. T. Al Abbas, N. A. W. Dutton, O. Almer, S. Pellegrini, Y. Henrion, and R. K. Henderson, "Backside illuminated SPAD image sensor with 7.83 μm pitch in 3D-stacked CMOS technology," in *IEEE International Electron Devices Meeting* (2016), pp. 811–814.
13. A. R. Ximenes, P. Padmanabhan, M.-J. Lee, Y. Yamashita, D.-N. Yang, and E. Charbon, "A modular, direct time-of-flight depth sensor in 45/65-nm 3-D-stacked CMOS technology," *IEEE J. Solid-State Circuits* **54**, 3203–3214 (2019).

14. R. K. Henderson, N. Johnston, S. W. Hutchings, I. Gyongy, T. Al Abbas, N. Dutton, M. Tyler, S. Chan, and J. Leach, "A 256×256 40 nm/90 nm CMOS 3D-stacked 120 dB dynamic-range reconfigurable time-resolved SPAD imager," in *IEEE International Conference on Solid-State Circuits Conference* (2019).
15. E. R. Fossum, "What to do with sub-diffraction-limit (SDL) pixels? A proposal for a gigapixel digital film sensor (DFS)," in *IEEE Workshop on Charge-Coupled Devices and Advanced Image Sensors* (2005), pp. 214–217.
16. E. R. Fossum, J. Ma, S. Masoodian, L. Anzagira, and R. Zizza, "The quanta image sensor: every photon counts," *Sensors* **16**, 1260 (2016).
17. F. Yang, Y. M. Lu, L. Sbaiz, and M. Vetterli, "Bits from photons: over-sampled image acquisition using binary Poisson statistics," *IEEE Trans. Image Process.* **21**, 1421–1436 (2012).
18. J. Ma, S. Masoodian, D. A. Starkey, and E. R. Fossum, "Photon-number-resolving megapixel image sensor at room temperature without avalanche gain," *Optica* **4**, 1474–1481 (2017).
19. A. Gnanasambandam, O. Elgendy, J. Ma, and S. H. Chan, "Megapixel photon-counting color imaging using quanta image sensor," *Opt. Express* **27**, 17298–17310 (2019).
20. J. Richardson, R. Walker, L. Grant, D. Stoppa, F. Borghetti, E. Charbon, M. Gersbach, and R. K. Henderson, "A 32×32 50 ps resolution 10 bit time to digital converter array in 130 nm CMOS for time correlated imaging," in *IEEE Custom Integrated Circuits Conference* (2009).
21. C. Veerappan, J. Richardson, R. Walker, D.-U. Li, M. W. Fishburn, Y. Maruyama, D. Stoppa, F. Borghetti, M. Gersbach, R. K. Henderson, and E. Charbon, "A 160×128 single-photon image sensor with on-pixel 55 ps 10 b time-to-digital converter," in *IEEE International Solid-State Circuits Conference* (2011).
22. A. Carimatto, S. Mandai, E. Venialgo, T. Gong, G. Borghi, D. R. Schaart, and E. Charbon, "A 67,392-SPAD PVTB-compensated multi-channel digital SiPM with 432 column-parallel 48 ps 17b TDCs for endoscopic time-of-flight PET," in *IEEE International Solid-State Circuits Conference* (2015).
23. M. Perenzoni, D. Perenzoni, and D. Stoppa, "A 64×64 -pixel digital silicon photomultiplier direct ToF sensor with 100Mphotons/s/pixel background rejection and imaging/altimeter mode with 0.14% precision up to 6km for spacecraft navigation and landing," in *IEEE International Solid-State Circuits Conference* (2016).
24. R. K. Henderson, N. Johnston, F. M. D. Rocca, H. Chen, D. D.-U. Li, G. Hungerford, R. Hirsch, D. McLoskey, P. Yip, and D. J. S. Birch, "A 192×128 time correlated SPAD image sensor in 40 nm CMOS technology," *IEEE J. Solid-State Circuits* **54**, 1907–1916 (2019).
25. C. Veerappan and E. Charbon, "A low dark count p-i-n diode based SPAD in CMOS technology," *IEEE Trans. Electron Devices* **63**, 65–71 (2016).
26. D. Bronzi, F. Villa, S. Bellisai, B. Markovic, S. Tisa, A. Tosi, F. Zappa, S. Weyers, D. Durini, W. Brockherde, and U. Paschen, "Low-noise and large-area CMOS SPADs with timing response free from slow tails," in *European Solid-State Device Research Conference (ESSDERC)* (2012), pp. 230–233.
27. F. Acerbi, G. Paternoster, A. Gola, N. Zorzi, and C. Piemonte, "Silicon photomultipliers and single-photon avalanche diodes with enhanced NIR detection efficiency at FBK," *Nucl. Instrum. Methods Phys. Res. A* **912**, 309–314 (2018).
28. N. A. W. Dutton, T. Al Abbas, I. Gyongy, F. M. D. Rocca, and R. K. Henderson, "High dynamic range imaging at the quantum limit with single photon avalanche diode-based image sensors," *Sensors* **18**, 1166 (2018).
29. I. M. Antolovic, C. Bruschini, and E. Charbon, "Dynamic range extension for photon counting arrays," *Opt. Express* **26**, 22234–22248 (2018).
30. S. Kawahito, I. A. Halin, T. Ushinaga, T. Sawada, M. Homma, and Y. Maeda, "A CMOS time-of-flight range image sensor with gates-on-field-oxide structure," *IEEE Sens. J.* **7**, 1578–1586 (2007).
31. W. van der Tempel, A. Ercan, T. Finatou, K. Fotopoulou, C. Mourad, F. Agavrioloie, S. Resimont, L. Cutrignelli, P. Thury, C. E. Medina, S. Xiao, J.-L. Loheac, J. Perhac, T. Van de Hauwe, V. Belokonskiy, L. Bossuyt, W. Aerts, M. Pauwels, and D. Van Nieuwenhove, "A 320×240 10 um CAPD ToF image sensor with improved performance," in *International Image Sensor Workshop* (2017).
32. C. S. Bamji, S. Mehta, B. Thompson, T. Elkhatab, S. Wurster, O. Akkaya, A. Payne, J. Godbaz, M. Fenton, V. Rajasekaran, L. Prather, S. Nagaraja, V. Mogallapu, D. Snow, R. McCauley, M. Mukadam, I. Agi, S. McCarthy, Z. Xu, T. Perry, W. Qian, V.-H. Chan, P. Adepu, G. Ali, M. Ahmed, A. Mukherjee, S. Nayak, D. Gampell, S. Acharya, L. Kordus, and P. O'Connor, "1 Mpixel 65 nm BSI 320 MHz demodulated TOF image sensor with 3.5 μ m global shutter pixels and analog binning," in *IEEE International Solid-State Circuits Conference* (2018).
33. D. Shin, F. Xu, F. N. C. Wong, J. H. Shapiro, and V. K. Goyal, "Computational multi-depth single-photon imaging," *Opt. Express* **24**, 1873–1888 (2016).
34. J. Haase, M. Beer, J. Ruskowski, and H. Vogt, "Multi object detection in direct time-of-flight measurements with SPADs," in *14th Conference on Ph.D. Research in Microelectronics and Electronics* (2018).
35. A. Kadambi, R. Whyte, A. Bhandari, L. Streeter, C. Barsi, A. Dorrington, and R. Raskar, "Coded time of flight cameras: sparse deconvolution to address multipath interference and recover time profiles," *ACM Trans. Graphics* **32**, 167 (2013).
36. F. Mochizuki, K. Kagawa, R. Miyagi, M.-W. Seo, B. Zhang, T. Takasawa, K. Yasutomi, and S. Kawahito, "Separation of multi-path components in sweep-less time-of-flight depth imaging with a temporally-compressive multi-aperture image sensor," *ITE Trans. Media Technol. Appl.* **6**, 202–211 (2018).
37. K. Kitano, T. Okamoto, K. Tanaka, T. Aoto, H. Kubo, T. Funatomi, and Y. Mukaigawa, "Recovering temporal PSF using ToF camera with delayed light emission," *IPSJ Trans. Comput. Vis. Appl.* **9**, 15 (2017).
38. E. Charbon, "Will avalanche photodiode arrays ever reach 1 megapixel?" in *International Image Sensor Workshop* (2007).
39. M. Perenzoni, M. Moreno-García, L. Gasparini, and N. Massari, "Time-resolved single-photon detectors: integration challenges in CMOS technologies," in *IEEE International Conference on IC Design and Technology* (2018).
40. J. M. Pavia, M. Wolf, and E. Charbon, "Measurement and modeling of microlenses fabricated on single-photon avalanche diode arrays for fill factor recovery," *Opt. Express* **22**, 4202–4213 (2014).
41. I. Gyongy, A. Davies, B. Gallinet, N. A. W. Dutton, R. Duncan, C. Rickman, R. K. Henderson, and P. A. Dalgarno, "Cylindrical microlensing for enhanced collection efficiency of small pixel SPAD arrays in single-molecule localisation microscopy," *Opt. Express* **26**, 2280–2291 (2018).
42. I. M. Antolovic, A. C. Ulku, E. Kizilkan, S. Lindner, F. Zanella, R. Ferrini, M. Schnieper, E. Charbon, and C. Bruschini, "Optical-stack optimization for improved SPAD photon detection efficiency," *Proc. SPIE* **10926**, 109262T (2019).
43. C. Niclass, C. Favi, T. Kluter, M. Gersbach, and E. Charbon, "A 128×128 single-photon image sensor with column-level 10-bit time-to-digital converter array," *IEEE J. Solid-State Circuits* **43**, 2977–2989 (2008).
44. S. Burri, Y. Maruyama, X. Michalet, F. Regazzoni, C. Bruschini, and E. Charbon, "Architecture and applications of a high resolution gated SPAD image sensor," *Opt. Express* **22**, 17573–17589 (2014).
45. S. Lindner, C. Zhang, I. M. Antolovic, M. Wolf, and E. Charbon, "A 252×144 SPAD pixel FLASH LiDAR with 1728 dual-clock 48.8 ps TDCs, integrated histogramming and 14.9-to-1 compression in 180nm CMOS technology," in *IEEE Symposium on VLSI Circuits* (2018).